PAPER

Check for updates

Two-step construction of KPDMS/Al₂O₃ ultra-barriers for wearable sensors†

Di Wen, Ruige Yuan, Fan Yang* and Rong Chen (iD) *

Wearable devices hold significant potential in healthcare and medical diagnostics. One major challenge in realizing this potential is the low barrier property of polymer substrates, which fail to withstand surrounding moisture and biofluids. In this work, a two-step strategy involving ALI followed by a UV-curing process is developed to fabricate a $K_{48}PDMS/Al_2O_3$ ultra-barrier with high barrier property of 7.82×10^{-5} g m^{-2} day^{-1} under stretching strain, representing one of the highest values among current works. Moreover, the $K_{48}PDMS/Al_2O_3$ barrier enables Ca-tested devices to exhibit extended operational lifetimes of up to 12 days in simulated rain. It also ensures the high sensitivity of strain sensors for real-time monitoring of health-related physiological signals, even when exposed to aggressive solutions such as PBS, KOH, and glucose. A clear "filling–cross-linking" mechanism is revealed, involving the filling of the void spaces within polymer chains followed by the cross-linking of polymer side chains to enhance the density of the hybrid layer. Adjusting porosity and functional group density ensures complete Al_2O_3 infiltration into the polymer. The cross-linking increases from 12.31% to 73.79% compared to the UV-curing process alone due to the presence of Al_2O_3, further enhancing the density of the hybrid layer and its barrier properties. The proposed strategy in our work shows great potential for providing highly reliable encapsulation for wearable electronics.

1. Introduction

Wearable devices can be adhered to the skin and even be implanted,[1] offering significant potential in healthcare and medical diagnostics.[2,3] Realizing this potential requires soft barrier substrates and encapsulation films that protect these wearable devices against moisture, biofluids, and water-based solutions from the surrounding environment.[4] However, common polymer substrates have large free volumes and high chain mobility, allowing moisture to permeate them readily.[5,6] Typically, these materials have a water vapor transmission rate (WVTR) that ranges from 1 to 100 g m^{-2} day^{-1}, whereas practical wearable electronic devices require a much lower WVTR value of below 10^{-4} g m^{-2} day^{-1} to ensure their stability.[7,8]

Various strategies, including use of polymer nanocomposites, polymer blending, and coating, aim to enhance the barrier properties of polymer substrates. Polymer nanocomposites and blending typically achieve barrier properties of around 10^{-3} g m^{-2} day^{-1},[9–13] which is insufficient to achieve long-

term stability for wearable devices. Coating, which involves depositing thin impermeable inorganic films chemically and physically on polymer substrates, shows potential for achieving highly flexible barriers.[14,15] One major challenge in achieving high barrier properties in polymer/inorganic composite structures is the interface instability caused by mismatches in modulus and CTE between the thin inorganic film and the polymer.[16,17]

Among the atomic-scale interface engineering methods, atomic layer infiltration (ALI) is considered one of the most effective methods to enhance interface stability through the construction of a gradient modulus structure, which comprises thin inorganic layers, hybrid layers, and a polymer layer. The thin inorganic films fabricated by ALI offer advantages such as high uniformity, conformity, precise thickness control at the sub-nanometer scale, and low-temperature deposition.[18] Importantly, the hybrid layer formed by filling the free empty spaces within the polymer with oxides not only efficiently mitigates modulus and thermal mismatches at the interface but also acts as a barrier layer against moisture. Furthermore, the density of these hybrid films is positively correlated with their barrier properties. Recently, ALI has been used to modify polymers including polyethylene naphthalate (PEN), polyethylene terephthalate (PET), polyimide (PI), and polydimethylsiloxane (PDMS), demonstrating its effectiveness in creating highly stable hybrid structures with excellent barrier properties.[18–22]

State Key Laboratory of Intelligent Manufacturing Equipment and Technology of School of Mechanical Science and Engineering, Huazhong University of Science and Engineering, Wuhan 430074, China.
E-mail: fan_yang@hust.edu.cn, rongchen@mail.hust.edu.cn

†Electronic supplementary information (ESI) available. See DOI: https://doi.org/10.1039/d4dt01893a

However, maintaining the high barrier properties of polymer substrates under deformation caused by human movement and exposure to aggressive solutions like sweat remains a challenge.

Here, we present a two-step strategy by introducing a UV-curing process after the ALI process to achieve high cross-linking density of K_nPDMS/Al_2O_3 ultra-barriers. The optimal barrier, $K_{48}PDMS/Al_2O_3$, demonstrates its ultra-barrier ability by sustaining high barrier properties (7.82×10^{-5} g m^{-2} day^{-1}) from unstrained to strain states. The $K_{48}PDMS/Al_2O_3$ ultra-barrier can enhance the water resistance of Ca-tested devices in rainfall scenarios. Additionally, the ultra-barrier of an encapsulated wearable strain sensor maintained its resistance after being soaked in aggressive solutions such as PBS solution, KOH, and glucose for a long time. Importantly, the encapsulated strain sensor illustrates changes in sensitivity under various actions of the human body, highlighting its potential for diverse wearable electronics applications. A clear "filling–cross-linking" mechanism is revealed, supported by QCM, FTIR, and SEM analyses. This mechanism involves the filling of void spaces within polymer chains followed by the cross-linking of polymer side chains to enhance the density of the hybrid structure. Notably, a synergistic effect occurs where infiltrated Al_2O_3 strengthens cross-linking, increasing it from 17.08% to 74.24% compared to the UV-curing process alone.

2. Experimental methods

2.1. Materials

3-Methacryloxypropylmethyldimethoxysilane (KH571), dibutyltin dilaurate (DBTDL), and SiO_2 nanoparticles (Hydrophilic-380 type) were purchased from Aladdin. Hydroxy-terminated polydimethylsiloxane (PDMS-OH) with an average molecular weight of 50 000 was purchased from Guangdong Weng Jiang Chemical Co., Ltd, China. Trimethylaluminum (TMA, 97.99999% purity) was obtained from Fornano.

2.2. Fabrication of functionalized PDMS films (K_nPDMS)

Unlike the traditional fabrication method for PDMS film (Sylgard 184), which requires thermal curing at elevated temperatures (>100 °C) and a long curing time of over 120 minutes,[23,24] the KPDMS substrates are synthesized via a solvent-free process by simply mixing the PDMS-OH, KH571, and SiO_2 nanoparticles at room temperature under fast curing for 2 min. The mass ratio of PDMS-OH, KH571, and SiO_2 is $5 : x : 1$ ($x = 1.6, 2.4, 3.2$). The prepared PDMS-based films are denoted as K_nPDMS, where n, which is equal to 32, 48, and 64, indicates the mass fraction of KH571. The KH571 is used as a cross-linking agent to react with PDMS-OH under the DBTL catalyst, forming the PDMS-based film,[25] where no films are obtained when KH571 is absent with only PDMS-OH, SiO_2, and DBTL catalyst being present in the precursor solution. The K_nPDMS was applied to PVA (polyvinyl alcohol) transfer paper using a scraper, resulting in a K_nPDMS film with an approximate thickness of 200 μm.

2.3. Atomic layer deposition (ALD) and atomic layer infiltration (ALI)

All the deposition processes were performed in a homemade viscous flow tube reactor. Metal–organic precursors and oxidants used in the ALD and ALI processes are trimethylaluminum (TMA) and deionized H_2O, respectively. The ALI chamber pressure is set to 0.6 Torr during the process with a constant 100 sccm flow of N_2 throughout to carry and purge the precursor vapors. The deposition temperature is 95 °C. The ALI process included 0.50 s of TMA pulse, 60 s of exposure time, 60 s of N_2 purge time, 0.50 s of H_2O pulse, 60 s of exposure time, and 60 s of purging. During the 60 s of exposure time, both the pump and gas flow are turned off, ensuring that the chamber is completely sealed. Consequently, only the initially introduced gases, including N_2 and precursor gas, remain. The ALD process included 0.50 s of TMA pulse, 60 s of N_2 purge time, 0.50 s of H_2O pulse, and 60 s of N_2 purge time.

2.4. UV-curing method

The UV-curing process is performed using a Full Features Flood UV lamp (Intelli-Ray 600, Uvitron, USA) with a UVA intensity of 150 mW cm^{-2}. The temperature of the UV light is 40 °C. UV light exposure times of 1, 5, and 10 minutes are employed in the study. $K_{64}PDMS$ is used as the sample due to its higher number of functional groups.

2.5. Fabrication and encapsulation of the porous graphene sensor

The porous graphene, employed as electrode material, is fabricated on a polyimide (PI) film using a laser direct writing (LDW) process, followed by the transfer of the $K_{48}PDMS$ film based on differential adhesion. The $K_{48}PDMS$ film serves as a top layer and bottom substrate, and the porous graphene strain sensor encapsulated by the $K_{48}PDMS/Al_2O_3$ barrier is prepared through the ALI treatment and UV-curing process.

2.6. Characterization of PDMS films

The thickness of pristine K_nPDMS ($n = 32, 48, 64$) and K_nPDMS/Al_2O_3 barriers are measured using an ultra-depth 3D microscope (DSX 510, Olympus) and an ellipsometer (SE, J.A. Woollam M2000). The FTIR spectra of the pristine K_nPDMS and K_nPDMS/Al_2O_3 barriers were recorded using a Nicolet iS 10 FTIR spectrometer (Thermo Fisher Scientific) with a diamond crystal ATR cell, at a resolution of 4 cm^{-1} over the 4000 to 400 cm^{-1} wavenumber range. The conversions of the double bonds of the K_nPDMS/Al_2O_3 barriers after exposure to UV treatment are calculated as follows:

$$DC(\%) = \frac{A_0 - A_t}{A_0} \times 100\%$$

where DC is the percentage conversion of double bonds at time t, A_0 is the peak area before UV treatment, and A_t is the peak area at time t after UV treatment.

The transparency is analyzed by UV–vis transmittance (Lambda 35, UV–Vis Spectrometer) in the range from 380 to 800 nm. The CTE is determined using a thermal-mechanical analysis (TMA, Q400) instrument under an N_2 atmosphere with a fixed load of 0.05 N. The temperature range is set from 50 °C to 400 °C, with a heating rate of 5 °C min^{-1}. The density of K$_n$PDMS was determined using volumetric displacement, and the porosity was calculated from the bulk density (ρ_b) and particle density (ρ_p): ($\varepsilon = 1 - \rho_b/\rho_p$).[26] The surface images of the K$_n$PDMS/A$_2$O$_3$ barrier (n = 32, 48, 64) before and after stretching are characterized with the ultra-depth 3D microscope (DSX 510, Olympus). The element line analysis of the K$_n$PDMS/Al$_2$O$_3$ barriers are characterized with a field emission scanning electron microscope (FE-SEM, Helios Nanolab G3 CX, FEI) equipped with an energy-dispersive X-ray (EDX) spectrometer. Mass gains are measured *in situ* using a quartz crystal monitor (QCM) system. A commercial stretching test machine is used to uniaxially stretch the K$_n$PDMS/Al$_2$O$_3$ barriers at ambient temperature. The barrier properties of the prepared thin films are measured according to the WVTR, estimated by using a Ca test at 30 °C and 70% R.H. Utilizing the activation energy of the Al$_2$O$_3$ thin film (50.8 kJ mol^{-1})[27] and the Arrhenius equation,[28] an acceleration factor of 2.65 is utilized to convert the WVTR values at 30 °C and 70% RH into values under ambient conditions (25 °C and 50% RH).

3. Results and discussion

3.1. Characterization of K$_n$PDMS substrates

A series of K$_n$PDMS (n = 32, 48, 64) substrates with adjustable physical properties, including modulus, CTE, and density/porosity were fabricated. As shown in Fig. 1a, the modulus of K$_n$PDMS is 1.86 MPa, 2.14 MPa and 2.71 MPa and breaking elongation is 197.6, 181.3% and 102% for K$_{32}$PDMS, K$_{48}$PDMS, and K$_{64}$PDMS, respectively. Fig. 1b reveals a reduction in the CTE of K$_n$PDMS with an increasing mass fraction of KH571. As shown in Fig. S1,† the FTIR spectra of the K$_n$PDMS films display a peak at 1008 cm^{-1} that corresponds to Si–O–Si stretching of PDMS, and three peaks at 1202 cm^{-1}, 1636 cm^{-1}, and 1718 cm^{-1} that are attributed to the stretching vibrations of –C–O, –C=O and –C=C groups of KH571,[29,30] respectively. These findings demonstrate the cross-linking reaction between KH571 and PDMS, resulting in the introduction of functional groups (C=C, C=O) into the PDMS chain. As illustrated in Fig. 1c, as the mass fraction of KH571 increases, the density of the K$_n$PDMS substrate increases, while the porosity exhibits an inverse trend. The porosity of K$_n$PDMS is 6.8%, 3.38%, and 1.99% for the K$_{32}$PDMS, K$_{48}$PDMS, and K$_{64}$PDMS, respectively. Fig. 1d demonstrates that all K$_n$PDMS substrates exhibit optical transparency in the visible region (380–780 nm), with an optical transmittance exceeding 86%. In summary, the
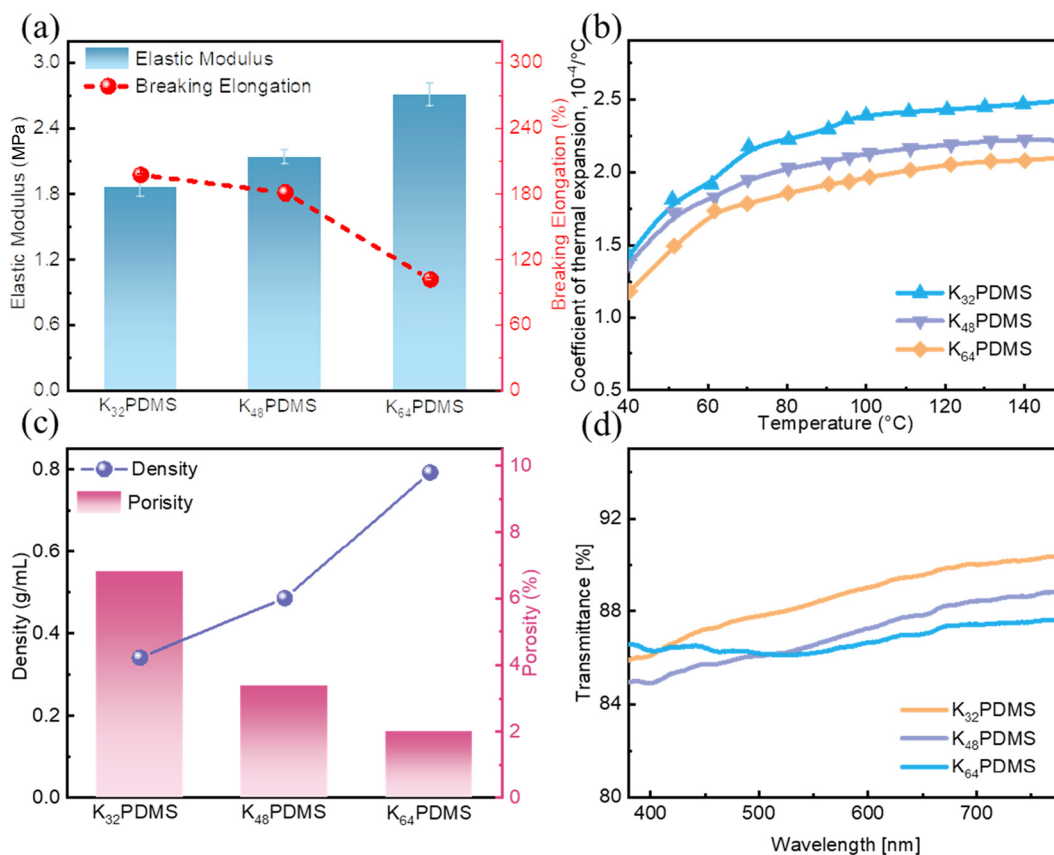

Fig. 1 The K$_n$PDMS films with engineered physical properties. (a) Elastic modulus and breaking elongation. (b) CTE. (c) Density and porosity. (d) Transmission.

K$_n$PDMS substrates, which are highly stretchable and transparent through the room temperature fabrication method, demonstrate promise as soft substrates for wearable electronics; the only drawback is their low barrier property, as shown in Fig. S2.†

3.2. Achieving high barrier property for K$_n$PDMS/Al$_2$O$_3$ barriers

A two-step strategy involving atomic layer infiltration (ALI) followed by a UV-curing process has been developed to enhance the barrier property of the K$_n$PDMS (n = 32, 48, 64) substrates, as illustrated in Fig. 2a. Fig. 2b demonstrates that the barrier property of K$_n$PDMS reaches 10^{-3} g m^{-2} day^{-1} after the ALI treatment, and further enhancements to $10^{-4}/10^{-5}$ g m^{-2} day^{-1} are achieved through additional UV-curing processes. Specifically, the WVTR is 1.71×10^{-4} g m^{-2} day^{-1}, 1.25×10^{-4} g m^{-2} day^{-1}, and 3.59×10^{-5} g m^{-2} day^{-1} for K$_{32}$PDMS, K$_{48}$PDMS and K$_{64}$PDMS, respectively, which improved by 4 to 5 orders of magnitude the WVTR of pristine K$_n$PDMS ($\sim$1 g m^{-2} day^{-1}). Fig. 2c shows that increasing the ALI cycles enhances the barrier properties of K$_n$PDMS/Al$_2$O$_3$ (n = 32, 48) barriers, but reduces the barrier properties of the K$_{64}$PDMS/Al$_2$O$_3$ barrier. With 130 ALI cycles, the WVTR barrier properties achieve values of 9.11×10^{-5} g m^{-2} day^{-1} for K$_{32}$PDMS/Al$_2$O$_3$ and 7.30×10^{-5} g m^{-2} day^{-1} for K$_{48}$PDMS/Al$_2$O$_3$. In contrast, the K$_{64}$PDMS/Al$_2$O$_3$ barrier exhibits a WVTR of 6.04×10^{-4} g m^{-2} day^{-1}. The decline after 130 cycles is due to the Al$_2$O$_3$ for the K$_{64}$PDMS/Al$_2$O$_3$ barrier exceeding a critical thickness, leading to reduced tensile strength and increased stress-induced cracking.[31,32] As shown in Fig. 2d, the WVTR of the K$_{64}$PDMS/Al$_2$O$_3$ barrier first decreases and then increases with the increase of curing time, achieving optimal barrier properties with a lower WVTR of 3.59×10^{-5} g m^{-2} day^{-1} at a curing time of 1 min. Therefore, a UV-curing time of 1 minute was employed for all UV-curing experiments, unless otherwise specified.

3.3. Potential of the K$_{48}$PDMS/Al$_2$O$_3$ ultra-barrier for wearable devices

The barrier for encapsulating wearable electronics is inevitably exposed to mechanical deformations during operation, making it crucial that the stability of the barrier is maintained under conditions such as bending and stretching. Fig. 3a demonstrates the excellent flexibility of K$_n$PDMS/Al$_2$O$_3$ barriers (n = 32, 48) with 130 ALI cycles. While K$_n$PDMS with 100 ALI cycles shows good flexibility with minimal WVTR change (Fig. S3a†), it is less flexible than K$_n$PDMS with 130 ALI cycles, as shown by the larger WVTR increase after stretching (Fig. S3b†). For K$_n$PDMS (n = 32, 48) with both 100 and 130 ALI cycles, no cracks are observed before or after stretching, as shown in Fig. S4 and S5.† In contrast, visible cracks in K$_{64}$PDMS with 130 ALI cycles after stretching (Fig. S5c†) are due to excessive thickness, correlating with the WVTR changes. In particular, the WVTR of the K$_{48}$PDMS/Al$_2$O$_3$ optimal barrier with 130 ALI cycles and UV-curing time of 1 min remains nearly unchanged, at 7.82×10^{-5} g m^{-2} day^{-1}, after 1% stretching. During stretching, the thin film extends uniformly along the stress direction, resulting in a uniform
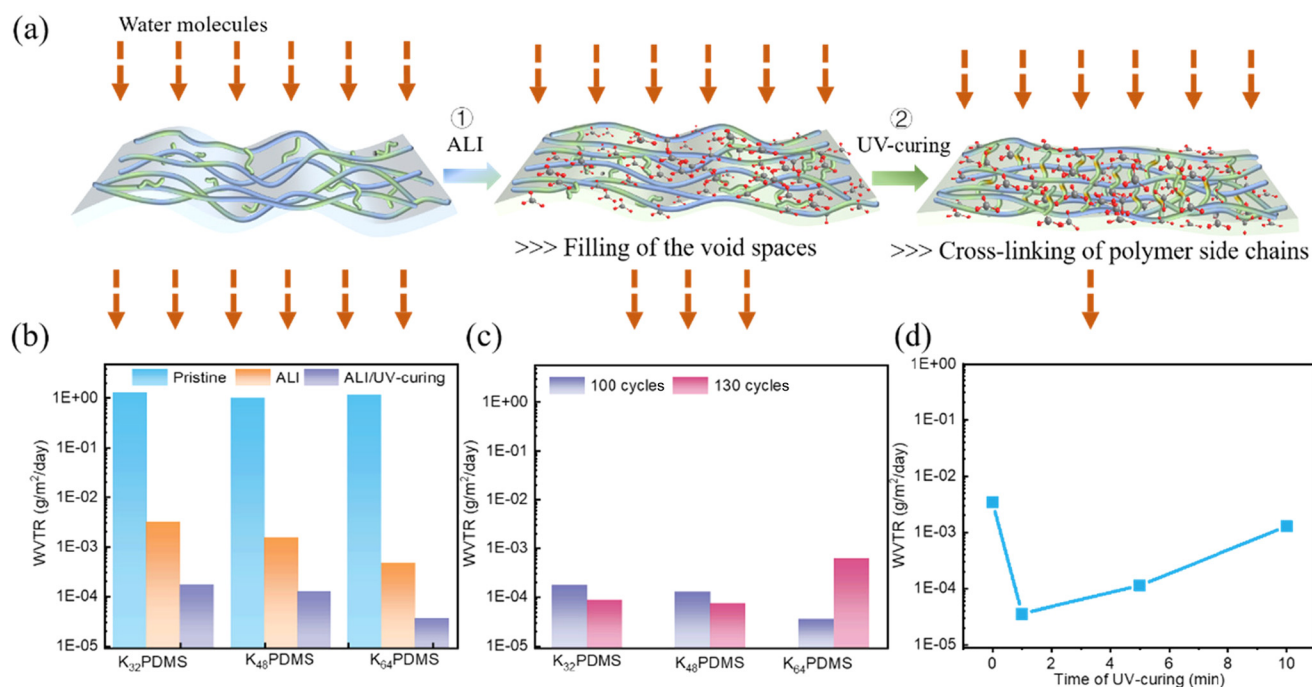

Fig. 2 Achieving high barrier properties in the K$_n$PDMS through ALI followed by UV-curing. (a) Synthetic route. (b) Process impact on barrier properties under 1 min of UV-curing time and 100 ALI cycles. (c) Effect of ALI cycle number on the barrier properties under 1 min of UV-curing time. (d) Effect of UV-curing time on the barrier properties for K$_{64}$PDMS treated with 100 cycles ALI.
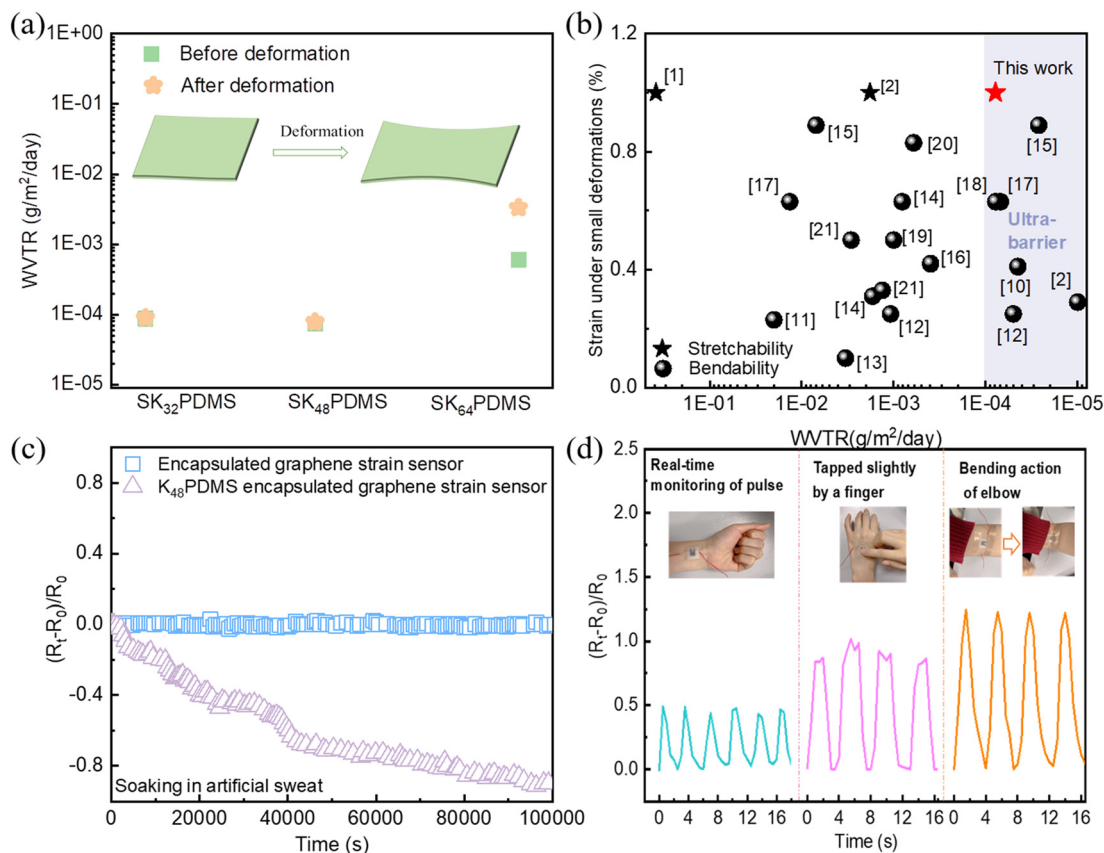
Fig. 3 Potential of the $K_{48}PDMS/Al_2O_3$ ultra-barrier for wearable electronics. (a) Deformation impact on barrier properties with 130 ALI cycles and 1 min of UV-curing time. (b) Literature summary of barrier properties and flexibility for various barriers, covering a wide range of bendable radii (30 mm to 1.75 mm). (c) Stability testing of an encapsulated strain sensor with/without PBS. (d) Real-time monitoring of pulse, slight finger tapping, and elbow bending actions.

stress distribution that requires greater flexibility compared to bending deformation.[33] Fig. 3b and Table S1† illustrate the superior barrier properties of $K_{48}PDMS/Al_2O_3$ while maintaining stretchability, contrasting with most other studies that focus on improving barrier properties while maintaining bendability, covering a wide range of bendable radii from 30 mm to 1.75 mm. Additionally, it demonstrates high barrier properties compared to reported stretchable barriers under the same strain.

The encapsulation performance of the $K_{48}PDMS/Al_2O_3$ ultra-barrier in practical weather situations was evaluated by exposing encapsulated Ca-tested devices to intermittent water, simulating rainfall scenarios. The results, as depicted in Fig. S6,† demonstrate significant improvements in the stability of encapsulated Ca-tested devices, with an extended operational lifetime of up to 12 days compared to instant inactivation observed in unencapsulated devices. Additionally, even after being subjected to 1% stretching, $K_{48}PDMS/Al_2O_3$ ultra-barrier-encapsulated Ca-tested devices exhibit similar decay behavior, indicating high barrier properties and flexibility, as illustrated in Fig. S7.† The $K_{48}PDMS/Al_2O_3$ ultra-barrier ensures that 90% normalized conductance is preserved in Ca-tested devices after 16 days of operation without exposure to

water. As shown in Fig. S8,† the $K_{48}PDMS/Al_2O_3$ ultra-barrier effectively prevents PBS penetration for 115 h at pH 7.4, in contrast to the rapid color change in Ca dots encapsulated within $K_{48}PDMS$. Fig. S9 and Table S2† indicate that devices encapsulated with $K_{48}PDMS/Al_2O_3$, when soaked in PBS solution, display a longer lifetime compared to those devices encapsulated with barriers such as single thin films, nanolaminates, polymer/thin films, and polymer/nanolaminates fabricated by ALD. This demonstrates that $K_{48}PDMS/Al_2O_3$ also effectively restricts ion diffusion.

The potential application of the $K_{48}PDMS/Al_2O_3$ ultra-barrier in wearable electronics is demonstrated by its high stability in a carbon-based strain sensor under challenging environmental conditions. Fig. S10† shows the synthetic route of the $K_{48}PDMS/Al_2O_3$ ultra-barrier encapsulated porous graphene sensor, and the $K_{48}PDMS/Al_2O_3$ ultra-barrier serves as a top encapsulation thin film and bottom flexible substrate. Fig. 3c demonstrates that the strain sensor encapsulated with $K_{48}PDMS$ film experiences decreased resistance after soaking in PBS solution, while the sensor encapsulated with the $K_{48}PDMS/Al_2O_3$ ultra-barrier maintains steady resistance. The encapsulated strain sensor also exhibits stability after exposure to KOH and glucose for 24 hours, as shown in Fig. S11.†

Additionally, as shown in Fig. 3d, the encapsulated strain sensor possesses high sensitivity under various conditions, such as pulse signal monitoring by attaching the sensor on the radial artery of the wrist, the response to slight tapping by a finger, and the response to the bending action of the elbow. Additionally, Fig. S12† indicates the high sensitivity of the encapsulated strain sensor under different bending actions of a human finger. In summary, the $K_{48}PDMS/Al_2O_3$ ultra-barrier maintains high barrier properties under deformation caused by human movement, ensuring the stability of wearable devices for real-time monitoring of health-related physiological signals even when exposed to aggressive solutions such as sweat, glucose, and base solutions.

3.4. Examining the roles of ALI and UV-curing in the KPDMS/Al_2O_3 barrier

The roles of ALI and UV-curing in enhancing the barrier property were investigated using *in situ* QCM, SEM, and FTIR techniques. Initially, the influence of growth behavior of Al_2O_3 on K_nPDMS (n = 32, 48, 64) substrates in the ALI process was monitored using the *in situ* QCM method. As shown in Fig. 4a, the ALI growth of Al_2O_3 for K_nPDMS can be divided into two stages based on the mass gain per cycle: the infiltration stage

and the deposition stage. During the infiltration stage, the mass gain per cycle initially increases and then decreases. This initial increase corresponds to the formation and growth of Al_2O_3 clusters, while the subsequent decrease is attributed to the closure of internal pores by the formed Al_2O_3.[22,34] For K_nPDMS substrates, the mass gain per cycle is similar during the deposition stages, stabilizing at approximately 40 ng per cm^2 per cycle. It is also found that the cycles required to achieve maximum Al_2O_3 infiltration differ, with $K_{64}PDMS$ reaching the highest infiltration in fewer cycles (4 cycles) compared to $K_{32}PDMS$ (7 cycles) and $K_{48}PDMS$ (5 cycles). This can be explained by $K_{64}PDMS$ having more reactive functional groups, such as carbonyl groups, which facilitate the entrapment of precursors. Additionally, the growth behavior of Al_2O_3 on optimal $K_{48}PDMS$ substrates in the ALD process was monitored using *in situ* QCM. As shown in Fig. S13a,† the total mass change on $K_{48}PDMS$ in ALI (2414.1 ng cm^{-2}) is significantly greater than in ALD (745.89 ng cm^{-2}). Fig. S13b† shows that the mass gain per cycle stabilizes at approximately 11.3 ng cm^{-2} for ALD, compared to 40 ng cm^{-2} for ALI. These results demonstrate that the holding time in ALI improves Al_2O_3 infiltration and increases nucleation sites, leading to a higher overall mass gain.
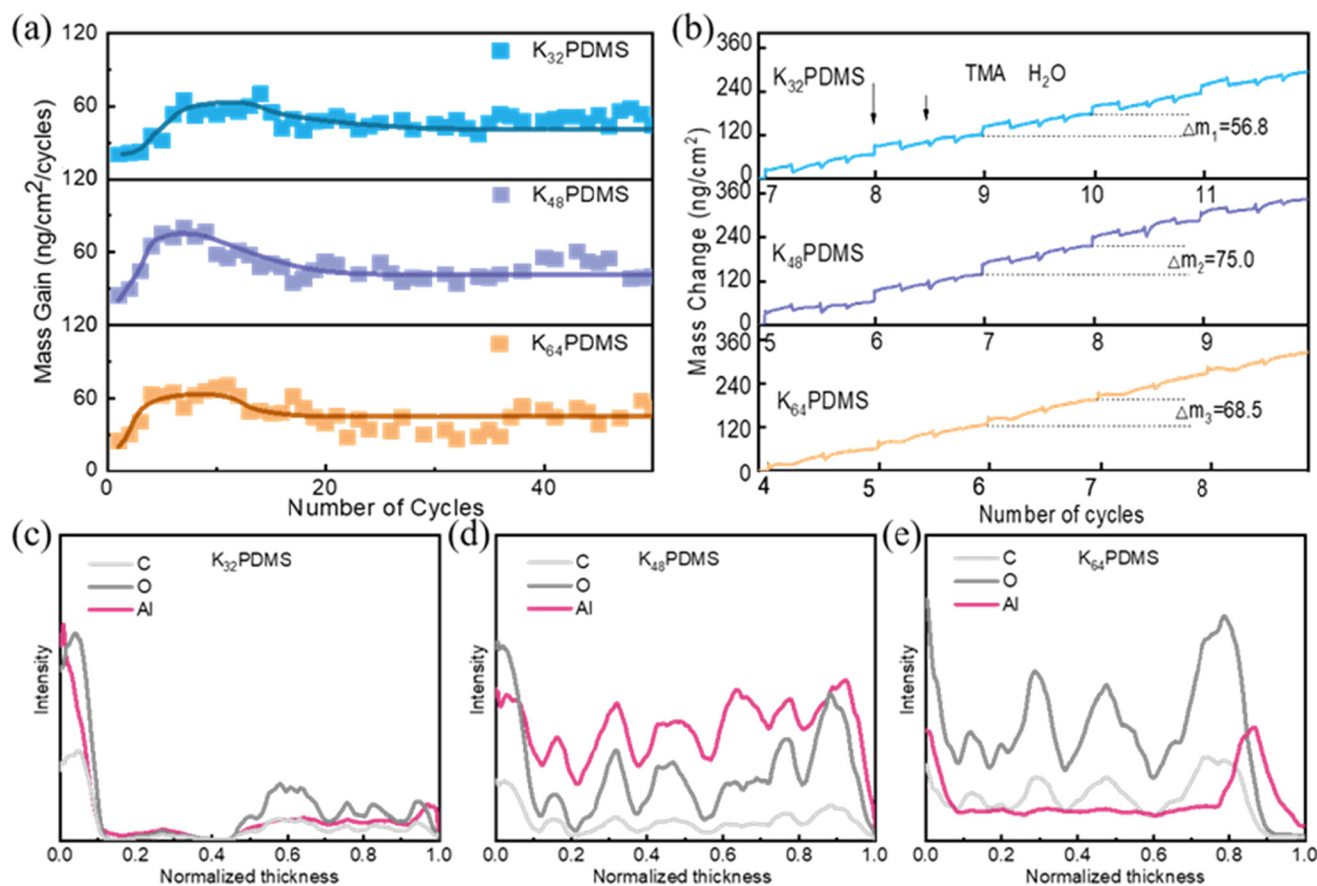

Fig. 4 The enhanced mechanism of barrier property in the ALI process. (a) QCM measurement of ALI processes on K_nPDMS. (b) The mass gain per cycle during the initial infiltration stage begins with the onset of maximum Al_2O_3 infiltration. (c–e) Element line-scan analysis of K_nPDMS treated with 100 ALI cycles.

Fig. 4b shows the different mass gains per cycle in the initial infiltration stage, with average mass gains per cycle of 56.8 ng per cm^2 per cycle, 75 ng per cm^2 per cycle, and 68.5 ng per cm^2 per cycle, for K$_{32}$PDMS, K$_{48}$PDMS and K$_{64}$PDMS, respectively. The highest Al$_2$O$_3$ infiltration of K$_{48}$PDMS enhances the density of the hybrid structure. The different Al$_2$O$_3$ infiltration amounts are determined by the density/porosity and functional group number of K$_n$PDMS.[35] Fig. S14† shows the elemental mapping in cross-sectional SEM images, with EDS data revealing the coexistence of Al, O, and C, demonstrating the infiltration of Al$_2$O$_3$ into the K$_n$PDMS. Furthermore, the distribution of the Al element throughout the cross-section was evaluated using the line-scan method. As shown in Fig. 4(c–e) and Fig. S15,† a higher normalized intensity of the Al element is observed throughout the cross-section for K$_{48}$PDMS, while for K$_{32}$PDMS and K$_{64}$PDMS, the Al element is only found on the surface and subsurface of the polymers. These results indicate that by adjusting the amount of KH571, full Al$_2$O$_3$ infiltration in K$_{48}$PDMS polymer can be achieved, resulting in higher density of the hybrid layer and barrier properties.

Furthermore, the bonding mode in the ALI process and UV-curing process is evaluated through FTIR analysis. K$_{48}$PDMS is selected as the representative sample due to its optimal per-
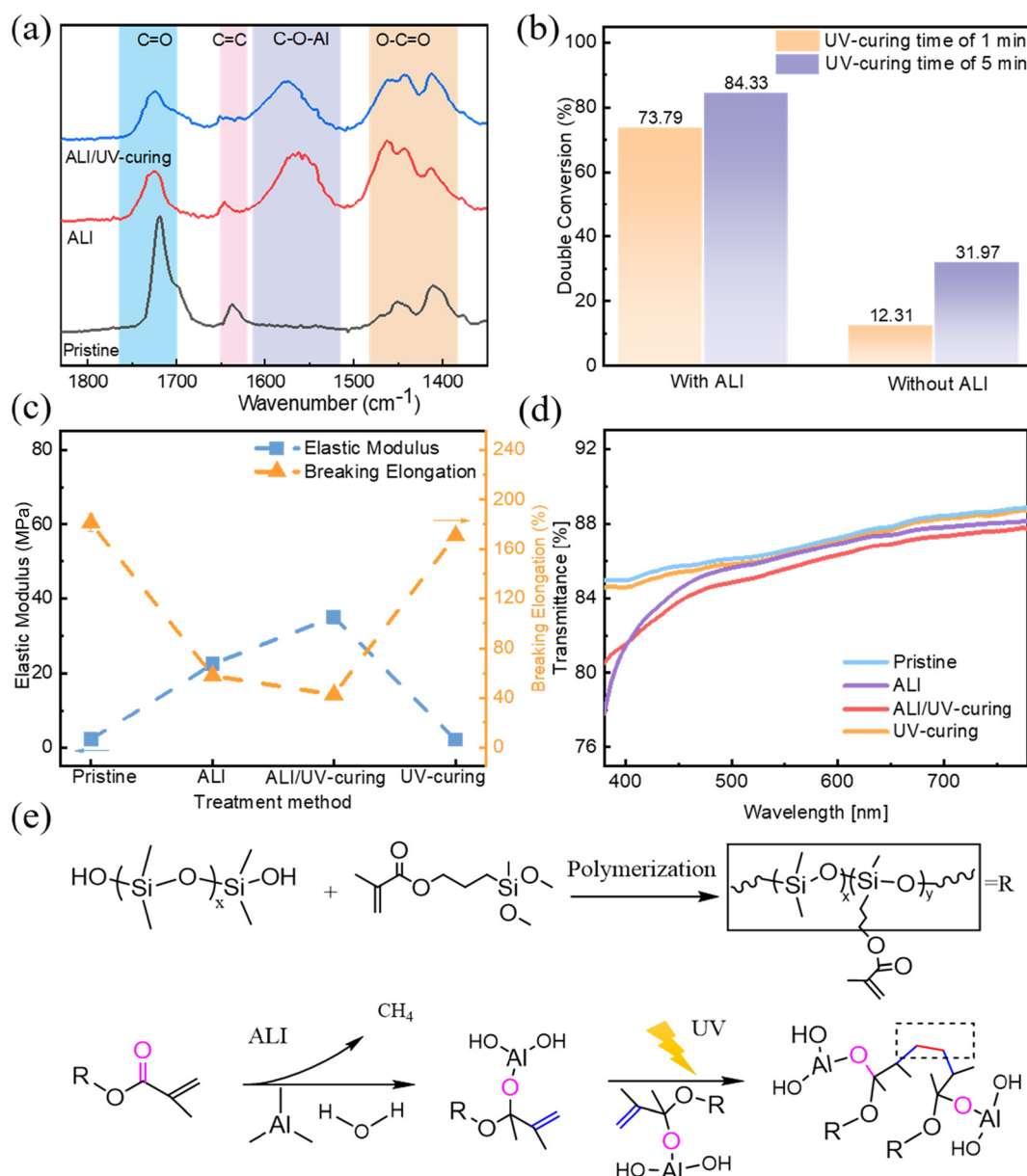

Fig. 5 The enhanced mechanism during the ALI and UV-curing process. (a) Bonding mode in FTIR spectra. (b) Cross-linking of polymer side chains with and without ALI during UV-curing. (c) Enhanced mechanical property. (d) Transmittance. (e) Schematic representation of the "filling–cross-linking" mechanism.

formance. Fig. 5a shows the FTIR spectra of $K_{48}PDMS$ after ALI and UV-curing. It is observed that red-shifted features correspond to a decrease in the C=O peak at 1718 cm^{-1}, and blue-shifted features of the ester C–O bond at 1202 cm^{-1} for the $K_{48}PDMS$ after the ALI process, compared to the FTIR of the pristine $K_{48}PDMS$ film. Additionally, two new peaks at 1558 cm^{-1} and 838 cm^{-1} are observed after the ALI process, correlated with C–O–Al and Al–O, respectively. These findings suggest that Al_2O_3 fills the voids within the polymer chain and reacts with C=O and C–O in polymer chains to enhance the density of the organic/inorganic hybrid layer.[36] Additionally, the increase in the C–O peak area is attributed to the formation of C–O–Al–OH from the reaction between C=O and TMA.[37] Notably, there is a significant decrease in the number of C=C groups, as indicated at 1646 cm^{-1}, after UV light exposure followed by the ALI process.

FTIR spectra after the UV-curing process with or without the ALI process are illustrated in Fig. S16 and S17† and clearly highlight the effect of the ALI process. Based on the change in the C=C peak area, the conversion rates of C=C (free radical polymer rate) after UV-curing with the ALI process for 1 minute and 5 minutes are determined to be 73.79% and 84.33%, respectively, whereas those without the ALI process for 1 minute and 5 minutes are 12.31% and 31.97% respectively, as illustrated in Fig. 5b. The higher conversion rates of C=C observed after UV exposure with the ALI process compared to those without ALI are attributed to the interaction between infiltrated Al_2O_3 and the C=O groups, which disrupts the conjugated structure (–C=O–C=C–), leading to an increased electron density of carbon (C=C). This makes it more susceptible to the generation of free radicals under radiation.[38]

The difference in cross-linking after UV-curing with or without the ALI process is also evidenced to various extents by changes in mechanical properties, transmission and the barrier property. Fig. 5c reveals that the elastic modulus of $K_{48}PDMS$ increases from 22.45 MPa to 35.06 MPa after ALI and ALI/UV-curing, respectively, showing a 993% and 1451% increase compared to pristine $K_{48}PDMS$. A similar trend is observed in K_nPDMS (n = 32, 64), with an increase in elastic modulus and a decrease in breaking elongation after the ALI process, as illustrated in Fig. S18.† Conversely, the elastic modulus remains nearly unchanged after UV-curing alone compared to pristine $K_{48}PDMS$. Similarly, a decrease in breaking elongation is observed after the ALI and ALI/UV-curing processes for the $K_{48}PDMS$ ultra-barrier, while it remains almost unchanged after UV-curing alone compared to pristine $K_{48}PDMS/Al_2O_3$ films. As shown in Fig. 5d, there was a notable decrease in transmission after UV-curing following the ALI process compared to the almost unchanged transmission after UV-curing alone. Fig. S19† shows the barrier properties of $K_{48}PDMS$ before and after UV-curing, ALI treatment, and combined ALI/UV-curing. The UV-curing alone yields barrier properties similar to pristine $K_{48}PDMS$, while the combined ALI and UV-curing process achieves the highest barrier property. Fig. 5e illustrates the "filling–cross-linking" reaction mecha-

nism. Initially, KH571 doping endows PDMS with functional groups such as C=O and C=C, facilitating the infiltration of Al_2O_3 into the polymer voids with strong bonding *via* C–O–Al, forming the organic/inorganic hybrid layer. Subsequently, infiltrated Al_2O_3 promotes the free-radical polymerization of C=C during the UV-curing process to further enhance the density of the organic/inorganic layer, thereby exhibiting high barrier properties.

4. Conclusions

In summary, K_nPDMS/Al_2O_3 ultra-barriers are fabricated through ALI followed by a UV-curing process. The optimal barrier, $K_{48}PDMS/Al_2O_3$, maintains the highest barrier property with a WVTR of 10^{-5} g m^{-2} day^{-1} under stretching. The $K_{48}PDMS/Al_2O_3$ ultra-barrier ensures that the wearable strain sensor maintains its high sensitivity to various health-related physiological signals even after prolonged exposure to aggressive solutions. Additionally, the $K_{48}PDMS/Al_2O_3$ ultra-barrier extends the operational lifetime of Ca-tested devices to 12 days in water and 4 days in PBS solution (pH 7.4). Complete Al_2O_3 infiltration is achieved in the polymer by effectively filling void spaces within the polymer chain and facilitating cross-linking of polymer side chains, enhancing the density of the hybrid layer and barrier properties. The $K_{48}PDMS/Al_2O_3$ ultra-barrier exhibits the highest barrier property, making it promising for applications in wearable devices in challenging environments.

Author contributions

Di Wen – conceptualization, investigation, formal analysis, writing – original draft. Ruige Yuan – validation, writing – review & editing. Fan Yang – conceptualization, writing – review & editing, supervision, funding acquisition. Rong Chen – writing – review & editing, supervision, project administration, funding acquisition.

Data availability

The data that support the findings of this study are available from the corresponding author upon reasonable request.

Conflicts of interest

The authors declare no conflict of interest.

Acknowledgements

References

1 E. Song, C. H. Chiang, R. Li, X. Jin, J. Zhao, M. Hill, Y. Xia, L. Li, Y. Huang, S. M. Won, K. J. Yu, X. Sheng, H. Fang, M. A. Alam, Y. Huang, J. Viventi, J. K. Chang and J. A. Rogers, *Proc. Natl. Acad. Sci. U. S. A.*, 2019, **116**, 15398–15406.

2 J. Zhang, J. Li, W. Cheng, J. H. Zhang, Z. Zhou, X. Sun, L. Li, J. G. Liang, Y. Shi and L. Pan, *ACS Mater. Lett.*, 2022, 577–599.

3 J. H. Kwon, E. G. Jeong, Y. Jeon, D. G. Kim, S. Lee and K. C. Choi, *ACS Appl. Mater. Interfaces*, 2019, **11**, 3251–3261.

4 Y. Liu, Q. Yu, L. Yang and Y. Cui, *Adv. Mater. Technol.*, 2023, **8**, 2200853.

5 M. Mariello, K. Kim, K. Wu, S. P. Lacour and Y. Leterrier, *Adv. Mater.*, 2022, **34**, 2201129.

6 Y. Li, Y. Xiong, H. Yang, K. Cao and R. Chen, *J. Mater. Res.*, 2020, **35**, 681–700.

7 G. Dennler, C. Lungenschmied, H. Neugebauer, N. S. Sariciftci and A. Labouret, *J. Mater. Res.*, 2005, **20**, 3224–3233.

8 T. Yokota, P. Zalar, M. Kaltenbrunner, H. Jinno, N. Matsuhisa, H. Kitanosako, Y. Tachibana, W. Yukita, M. Koizumi and T. Someya, *Sci. Adv.*, 2016, **2**, 1–9.

9 K. Müller, E. Bugnicourt, M. Latorre, M. Jorda, Y. E. Sanz, J. M. Lagaron, O. Miesbauer, A. Bianchin, S. Hankin, U. Bölz, G. Pérez, M. Jesdinszki, M. Lindner, Z. Scheuerer, S. Castelló and M. Schmid, *Nanomaterials*, 2017, **7**, 74.

10 D. V. Houcke, S. Kumar and B. R. Kona, *RSC Adv.*, 2015, **5**, 63669–63690.

11 D. A. Kunz, J. Schmid, P. Feicht, J. Erath, A. Fery and J. Breu, *ACS Nano*, 2013, **7**, 4275–4280.

12 Z. Yang, H. Guo, C. Kang and L. Gao, *New J. Chem.*, 2021, **45**, 12945–12956.

13 Y. Zheng, L. Michalek, Q. Liu, Y. Wu, H. Kim, P. Sayavong, W. Yu, D. Zhong, C. Zhao, Z. Yu, J. A. Chiong, H. Gong, X. Ji, D. Liu, S. Zhang, N. Prine, Z. Zhang, W. Wang, J. B.-H. Tok, X. Gu, Y. Cui, J. Kang and Z. Bao, *Nat. Nanotechnol.*, 2023, **18**, 1175–1184.

14 J. H. Han, T. Y. Kim, D. Y. Kim, H. L. Yang and J. S. Park, *Dalton Trans.*, 2021, **50**, 15841–15848.

15 C. Janowitz, A. Mahmoodinezhad, M. Kot, C. Morales, F. Naumann, P. Plate, M. H. Zoellner, F. Bärwolf, D. Stolarek, C. Wenger, K. Henkel and J. I. Flege, *Dalton Trans.*, 2022, **51**, 9291–9301.

16 S. H. Jen, S. M. George, R. S. McLean and P. F. Carcia, *ACS Appl. Mater. Interfaces*, 2013, **5**, 1165–1173.

17 O. Graudejus, P. Görrn and S. Wagner, *ACS Appl. Mater. Interfaces*, 2010, **2**, 1927–1933.

18 Y. Li, D. Wen, Y. Zhang, Y. Lin, K. Cao, F. Yang and R. Chen, *Dalton Trans.*, 2021, **50**, 16166–16175.

19 M. D. Losego and Q. Peng, *Surf. Modif. Polym. Methods Appl*, 2019, pp. 135–159.

20 E. Cianci, D. Nazzari, G. Seguini and M. Perego, *Adv. Mater. Interfaces*, 2018, **5**, 1–10.

21 S. H. Kim, S. Y. Song, S. Y. Kim, M. W. Chang, H. J. Kwon, K. H. Yoon, W. Y. Sung, M. M. Sung and H. Y. Chu, *npj Flexible Electron.*, 2022, **6**, 1–6.

22 Y. Zhang, D. Wen, M. Liu, Y. Li, Y. Lin, K. Cao, F. Yang and R. Chen, *Adv. Mater. Interfaces*, 2022, **9**, 1–9.

23 B. Gong, J. C. Spagnola and G. N. Parsons, *J. Vac. Sci. Technol., A*, 2012, **30**, 01A156-1–01A156-5.

24 J. Huang, Y. Cai, C. Xue, J. Ge, H. Zhao and S. H. Yu, *Nano Res.*, 2021, **14**, 3636–3642.

25 C. Salazar-Hernández, M. Salazar-Hernández, R. Carrera-Cerritos, J. M. Mendoza-Miranda, E. Elorza-Rodríguez, R. Miranda-Avilés and C. D. Mocada-Sánchez, *Prog. Org. Coat.*, 2019, **136**, 105220.

26 J. Qiu, S. Khalloufi, A. Martynenko, G. Van Dalen, M. Schutyser and C. Almeida-Rivera, *Drying Technol.*, 2015, **33**, 1681–1699.

27 K. H. Yoon, H. S. Kim, K. S. Han, S. H. Kim, Y.-E. K. Lee, N. K. Shrestha, S. Y. Song and M. M. Sung, *ACS Appl. Mater. Interfaces*, 2017, **9**, 5399–5408.

28 T. S. Kwon, D. Y. Moon, Y. K. Moon, W. S. Kim and J. W. Park, *J. Nanosci. Nanotechnol.*, 2012, **12**, 3696–3700.

29 D. Li, F. Xu, Z. Liu, J. Zhu, Q. Zhang and L. Shao, *Appl. Surf. Sci.*, 2013, **266**, 368–374.

30 M. A. Velazco-Medel, L. A. Camacho-Cruz and E. Bucio, *Radiat. Phys. Chem.*, 2020, **171**, 108754.

31 J. Wu, F. Fei, C. Wei, X. Chen, S. Nie, D. Zhang, W. Su and Z. Cui, *RSC Adv.*, 2018, **8**, 5721–5727.

32 Y. Li, Y. Xiong, W. Cao, Q. Zhu, Y. Lin, Y. Zhang, M. Liu, F. Yang, K. Cao and R. Chen, *Adv. Mater. Interfaces*, 2021, **8**, 1–9.

33 J. Lv, G. Thangavel and P. S. Lee, *Nanoscale*, 2022, **15**, 434–449.

34 Q. Peng, Y. C. Tseng, Y. Long, A. U. Mane, S. DiDona, S. B. Darling and J. W. Elam, *Langmuir*, 2017, **33**, 13214–13223.

35 R. A. Nye, S. Wang, S. Uhlenbrock, J. A. Smythe and G. N. Parsons, *Dalton Trans.*, 2022, **51**, 1838–1849.

36 J. C. Spagnola, B. Gong, S. A. Arvidson, J. S. Jur, S. A. Khan and G. N. Parsons, *J. Mater. Chem.*, 2010, **20**, 4213–4222.

37 B. Gong, Q. Peng, J. S. Jur, C. K. Devine, K. Lee and G. N. Parsons, *Chem. Mater.*, 2011, **23**, 3476–3485.

38 T. Y. Lee, T. M. Roper, E. S. Jonsson, I. Kudyakov, K. Viswanathan, C. Nason, C. A. Guymon and C. E. Hoyle, *Polymer*, 2003, **44**, 2859–2865.